

Solar flare observations with the Radio Neutrino Observatory Greenland (RNO-G)

S. Agarwal¹, J. A. Aguilar², S. Ali¹, P. Allison³, M. Betts⁴, D. Besson¹, A. Bishop^{5,6}, O. Botner⁷, S. Bouma⁸, S. Buitink^{9,10}, M. Cataldo⁸, B. A. Clark¹¹, A. Coleman⁷, K. Couberly¹, S. de Kockere⁶, K. D. de Vries⁶, C. Deaconu¹², M. A. DuVernois⁵, C. Glaser⁷, T. Glüsenkamp⁷, A. Hallgren⁷, S. Hallmann^{*13}, J. C. Hanson¹⁴, B. Hendricks⁴, J. Henrichs^{13,8}, N. Heyer⁷, C. Hornhuber¹, K. Hughes³, T. Karg¹³, A. Karle⁵, J. L. Kelley⁵, M. Korntheuer^{2,6}, M. Kowalski^{13,15}, I. Kravchenko¹⁶, R. Krebs⁴, R. Lahmann⁸, U. Latif⁶, P. Laub⁸, C.-H. Liu¹⁶, M. J. Marsee¹⁷, Z. S. Meyers^{13,8}, M. Mikhailova^{*1}, C. Monstein²¹, K. Mulrey¹⁰, M. Muzio⁴, A. Nelles^{13,8}, A. Novikov¹⁸, A. Nozdrina¹, E. Oberla¹², B. Oeyen¹⁹, N. Punsuebsay¹⁸, L. Pyras^{13,8}, M. Ravn⁷, D. Ryckbosch¹⁹, F. Schlüter², O. Scholten^{6,20}, D. Seckel¹⁸, M. F. H. Seikh¹, J. Stoffels⁶, K. Terveer⁸, S. Toscano², D. Tosi⁵, D. J. Van Den Broeck^{6,9}, N. van Eijndhoven⁶, A. G. Vieregge¹², A. Vijai¹¹, C. Welling¹², D. R. Williams¹⁷, P. Windischhofer¹², S. Wissel⁴, R. Young¹, and A. Zink⁸

(Affiliations can be found after the references)

Received 2024

ABSTRACT

Context. The Radio Neutrino Observatory-Greenland (RNO-G), currently under construction at Summit Station, Greenland, seeks discovery of ultra-high energy neutrinos from the cosmos through their interactions in the ice. Thus far, seven of a planned total of 35 radio-frequency receiver stations (24 antennas/station) have been installed. They have been designed for sensitivity to impulsive radio signals with frequencies between 80 and 700 MHz, and continuously operate during the polar summer months with a trigger threshold for recording data close to the thermal floor.

Aims. The RNO-G science program extends beyond particle astrophysics to include radioglaciology and, as we show herein, solar physics, as well. Impulsive solar flare observations not only permit direct measurements of light curves, spectral content, and polarization on time scales significantly shorter than most extant dedicated solar observatories, but also offer an extremely useful above-surface calibration source, with pointing precision of order tens of arc-minutes.

Methods. Using the early RNO-G data from 2022 – 2023, observed flare characteristics are compared to well-established solar observatories. Also, a number of individual flares are used to highlight angular reconstruction and calibration methods.

Results. RNO-G observes signal excesses during solar flares reported by the solar-observing Callisto network and in coincidence with about 60% of the brightest excesses recorded by the SWAVES satellite, when the Sun is above the horizon for RNO-G. In these observed flares, there is significant impulsivity in the time-domain. In addition, the solar flares are used to calibrate the RNO-G absolute pointing on the radio signal arrival direction to sub-degree resolution.

Conclusions. RNO-G will continue to use the Sun as calibration source for all future stations. As a bright infinite-distance source, solar flares uniformly illuminate stations over distance scales of tens of kilometers, allowing simultaneous reconstruction, which may improve the solar capabilities of RNO-G further.

Key words. solar flares – radio telescopes – UHE neutrinos – calibration

1. Introduction

The Radio Neutrino Observatory in Greenland (RNO-G) experiment is currently under construction near Summit Station, with the goal of measuring astrophysical neutrinos with energies exceeding 10^{15} eV. In its final form, RNO-G will consist of an array of several hundreds of radio antennas embedded in the glacial ice of Greenland, sensitive to radio signals produced by an in-ice neutrino interaction. RNO-G is designed for nearly-continuous up-time, recording data whenever a radio signal can be identified above the (largely) thermal noise floor. The RNO-G frequency response covers the range 80 - 700 MHz, which also overlaps with solar radio-emission frequencies during flaring. Beyond its primarily particle astrophysics mission, RNO-G data provides insights into solar signals. Those signals must also be identified

as possible contamination to searches for radio emissions from down-coming cosmic rays. In addition, signals from the Sun also offer considerable utility as a tool to calibrate the instrument.

In this article we outline the instrumental capabilities of RNO-G, detail data taken during solar flares in 2022 and 2023, elaborate on time-domain characteristics of the signals, and show how solar signals are used within RNO-G for hardware verification. Fortunately, the construction of the RNO-G instrument has coincided with the most recent solar maximum, expected to peak in 2024.

1.1. RNO-G

The primary goal of RNO-G is the discovery of astrophysical neutrinos above PeV energies (Aguilar et al. 2021). These neutrinos are predicted to arise from interactions of ultra high-energy cosmic rays, particularly those particles having the high-

* E-mail: authors@rno-g.org, steffen.hallmann@desy.de, masha.mikhailova@icecube.wisc.edu

est known energy in the universe (Berezinsky & Zatsepin 1969; Stecker 1973) with material around their production sites (Waxman & Bahcall 1999) or with the cosmic microwave background (Engel et al. 2001). While firmly predicted, the neutrino flux level is as-yet unknown and a measurement will strongly constrain our understanding of the high energy universe (Halzen & Hooper 2002).

RNO-G will measure neutrinos by detection of radio emissions produced via the Askaryan mechanism (Askar'yan 1961). A neutrino interacting in ice produces a cascade of elementary particles; as the shower evolves, it acquires an overall negative charge owing to scattering of atomic electrons into the cascade, and depletion of shower positrons via annihilation. The (net negative) charge distribution produced in this cascade moves faster than the speed of light in the medium and thus gives rise to radio pulses of nanosecond-scale duration along a narrow cone-shaped emission profile (Zas et al. 1992), which then propagate through the radio-transparent ice to the antennas of RNO-G (Aguilar et al. 2022). Reconstructing the neutrino direction in sparsely instrumented radio-neutrino detectors is complicated by the fact that only a small portion of the emission cone is seen by the antennas. The well-defined position of the Sun can be used as a calibration source for the absolute pointing for the arrival direction of the signal. Note that for neutrinos it is essential to also determine which part of the cone was observed. The latter can be constrained by the polarization, amplitude distribution, and frequency spectrum of the signal which are the dominant sources of uncertainty for the angular resolution on the neutrino direction (Anker et al. 2020; Plaisier et al. 2023). For an overview of the in-ice radio technique and a review of other experimental efforts, see (Barwick & Glaser 2023).

RNO-G is based on an array layout, where the planned 35 stations are installed on a square grid with interstitial spacing of 1.25 km (Figure 1). Each station constitutes an independent and self-contained neutrino detector and consists of 24 antennas embedded in the ice. Each station combines log-periodic dipole antennas (LPDA) close to the surface with fat-dipoles (Vpol) and quad-slot antennas (Hpol) on instrumented strings down to 100 m below the surface. Construction began in 2021 with the commissioning of, and subsequent data collection for the first three stations. In 2022, four additional stations were added, so that during solar flares in this analysis up to seven stations were recording data. Construction will continue at least until 2026, adding new stations every year to reach 35 stations. Extensions beyond 35 stations are possible.

The stations are currently powered only with solar power, such that the instruments turn off during the dark polar night (see Figure 2), although battery buffering ensures operation extending until October of each year. Since neutrino sensitivity scales directly with up-time, future wind-power operation should improve lifetime, targeting an overall uptime of 80%; solar observations, of course, are possible only when the Sun is above the horizon (cf. Figure 2).

Following a trigger, recorded waveforms consist of 2048 samples written at a sampling rate of 3.2 GHz, resulting in 640 ns time windows for recorded events. (The sampling rate is planned to be lowered to 2.4 GHz for future seasons to extend the time-period captured.) Given the sensitivity of antennas and this sampling rate, the stations have an effective bandwidth of 80 MHz to 700 MHz with a frequency resolution of better than 1 MHz. Station timing is determined via GPS clocks, meaning the station trigger times are, in principle, accurate to ~ 10 ns.

There are several different types of triggers currently running on the RNO-G stations. The primary trigger uses signals

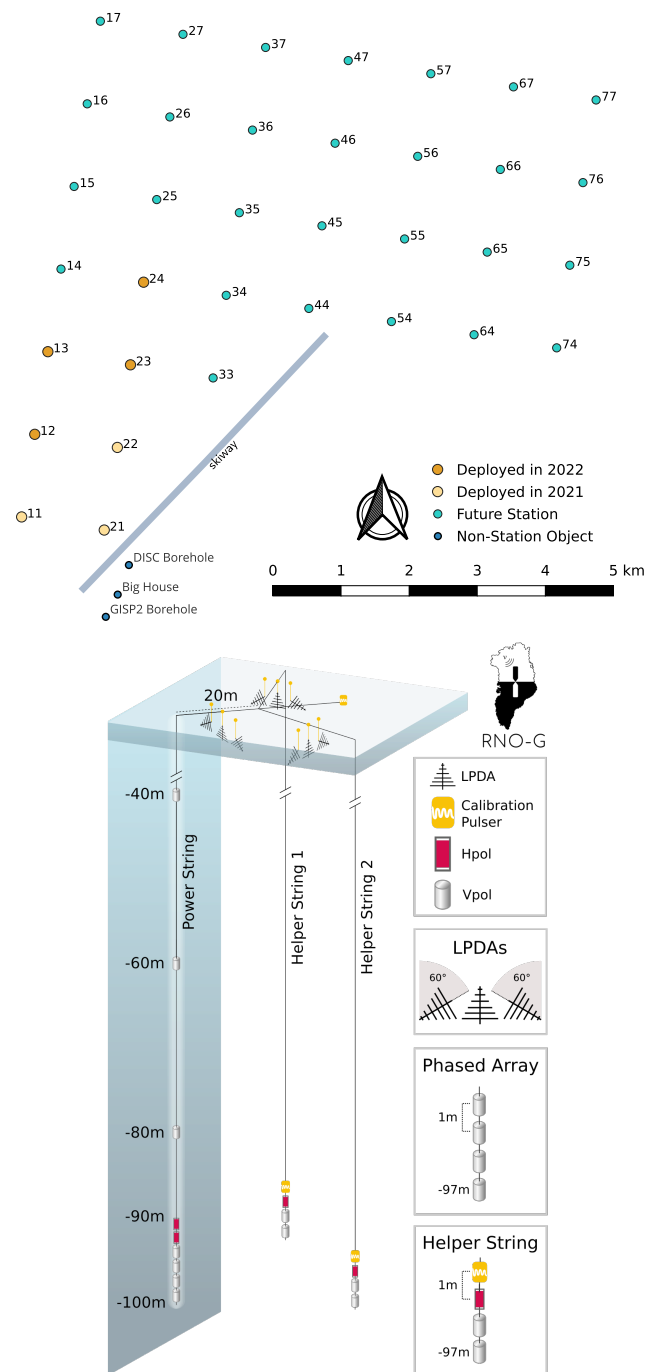


Fig. 1. Top: Planned positions of the stations of RNO-G. The seven installed stations are highlighted in different colors. The main building of Summit Station is denoted by *Big House*; also indicated is the landing strip for airplanes. Bottom: Schematic view of an RNO-G station. Each station has 24 antennas, either LPDA, Hpol or Vpol (see text for details). LPDAs are deployed in shallow trenches while Hpol and Vpol antennas are lowered into deep dry boreholes.

from the four Vpol antennas at the bottom of the power string. It is designed to trigger on the very small signals stemming from neutrino interactions (Allison et al. 2019) and tuned to a target trigger rate of 1 Hz. An auxiliary trigger formed by a combination of signals in the near-surface LPDAs targets a trigger rate of approximately 0.1 Hz. Thresholds on the separate trigger paths dynamically self-adjust by raising/lowering signal thresholds per

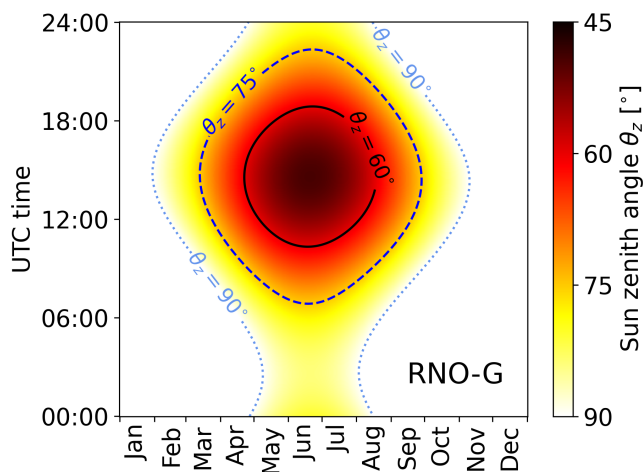


Fig. 2. Zenith position of the Sun observed from RNO-G. The Sun is above the horizon for the full day for 85 days of the year (May 10 to August 3). A minimum $\theta_z = 49^\circ$ is reached during solstice.

channel to achieve the pre-set target trigger rate. Consequently, during periods of high external noise such as solar bursts, the trigger rate will drop after the initial onset, as the threshold is raised once per second until the target rate is matched. In addition, a continuous and un-biased sample of *forced trigger* events is written out on fixed time intervals every 10 seconds, which guarantees continual monitoring of the ambient background.

We would like to highlight, that the upward facing LPDAs are intrinsically more sensitive to solar emission than the in-ice antennas because they are upward pointing. They thus have a substantially higher gain in the direction of the Sun compared to the antennas embedded deep in the ice. However, since the main purpose of RNO-G is neutrino detection, the LPDA-based trigger is only auxiliary and therefore not the main driver of the data-rate.

1.2. Solar Observations with RNO-G

Solar flares with accompanying radio-frequency emissions may arise via large prominences, or during periods of coronal mass ejections (CME). While the total energy output of the Sun is constant to within 0.1% (Kopp 2016) (dominated by infrared and optical wavelengths), the instantaneous power released in the radio and X-ray bands in a solar flare may exceed the background level by several orders of magnitude.

Observationally, solar flares are often classified via their X-ray emission, which are sorted according to their peak strength A, B, C, M, and X, with A being the smallest and X being the largest. Although related, there is no one-to-one correlation between X-ray and radio flares (Fletcher et al. 2011). Solar radio bursts are divided into five general classes I–V, based on their spectral and temporal characteristics; within these classes individual impulsive events exhibit considerable variation, e.g. Dulk (1985); Bastian et al. (1998); Wild & McCready (1950).

Type I bursts are related to active hot-spots on the solar surface. They are short (second-long) quasi-monochromatic radiation spikes with huge variation in intensity in the 80–200 MHz frequency range. They usually cluster as ‘noise storms’ which can last from a few hours up to a few days and sometimes feature a continuous underlying broadband emission. Although single

signals show no eminent drift in frequency, the radiation spikes tend to shift to lower frequencies during a storm.

Type II bursts are associated with electrons accelerated in the shock fronts at the leading edge of CMEs. They last a few minutes during which the narrow-band emission of the fundamental (harmonic) mode slowly drifts from ~ 150 (300) MHz to lower frequencies. Typical drift rates are ~ 0.05 MHz/s consistent with a shock wave propagating outwards from the solar surface at ~ 1000 km/s (Kumari et al. 2023).

Type III bursts are emitted by relativistic (~ 0.1 – $0.3 c$) electron beams travelling along open magnetic field lines during CME events. Compared to Type II, they are shorter (few seconds) and show a faster drift from up to ~ 1 GHz towards lower frequencies (up to ~ 100 MHz/s). Type III bursts may occur in isolation or in groups. Rarely, Type III bursts do not continue to drift to lower frequencies towards their end, but show an inverted ‘J’ or ‘U’ shape in their dynamic spectra. For these ‘J’ and ‘U’ subtypes, electrons do not escape along open magnetic field lines but instead propagate downwards along a closed loop within the solar corona (Maxwell & Swarup 1958).

The most relevant types of bursts for RNO-G are the most abundant type III and II based on their frequency content and duration. While type II bursts are long enough to appear in even the unbiased event sample of forced triggers, type III bursts need to surpass the trigger threshold to be identified in the data stream.

The two remaining types IV and V occur only rarely and never in isolation. They are not easily identified in RNO-G due to their broad-band structure and because of their long duration or low frequencies, respectively: Type IV is a smooth continuum of broad-band bursts. These flares begin 10 to 20 minutes after the flare maximum of some major flare events and can last for hours. Type V bursts are short-lived continuum noise at the lower frequency tail below 200 MHz that rarely follow a Type III burst.

The sample of 2535 reported Callisto bursts (see below) in the field of view for RNO-G in the 2022 and 2023 data is dominated by type III (89%) flares, followed by type II (4%), V (2%), IV (1%), and other miscellaneous RF noise fluctuations (4%). None of the few reported type I flares occurred in the RNO-G field of view during active data taking.

For RNO-G, the salient features of solar flare emissions are as follows. Radiation is emitted by relativistic electron beams (type III bursts) or travelling shock waves (type II bursts). The emission is at the electron plasma frequency (Langmuir wave frequency)

$$f_{pe} = \frac{1}{2\pi} \sqrt{\frac{e^2 n_e}{m_e \epsilon_0}} \approx 0.009 \sqrt{\frac{n_e}{\text{cm}^3}} \text{ MHz} \quad (1)$$

or its harmonics. Several models exist that describe the electron density as a function of height in the solar corona (extending into the solar wind and interplanetary space), e.g. Mann et al. (1999). With these, it is possible to (roughly) translate an observed frequency to distance above the solar surface. Using Equation 1 and the electron density profile, observed frequency drift rates df/dt can be converted to radial propagation velocities of the burst as well as height above the photosphere.

Generally, the emitted frequencies are lower further away from the Sun, and drift rates decrease faster at high frequencies due to the decreasing scale height of the plasma density as a function of solar radius. Given the lower frequency cutoff of the RNO-G amplifiers at ~ 80 MHz, radio signals beyond ~ 1.4 solar radii are not expected to be observed in RNO-G.

The angular diameter of the solar photosphere is 0.54° on the sky, although the solar spot, as viewed by RNO-G in-ice an-

tennas, compresses in elevation due to refraction at the ice-air boundary. Radio emission in the frequency range relevant for RNO-G is contained within a $\sim 1^\circ$ diameter. Hence, for RNO-G, radio pulses from solar flares arrive as a planar wave front from an infinitely far point-emitter, providing a unique calibration source to validate the pointing accuracy of the instrument.

Although plasma emission is the accepted mechanism behind type II and III solar flares and should imply strong circular polarization of the signal, type II and III typically show at most mild levels of circular polarization (Komesaroff 1958; Wentzel 1984).

1.3. Extant Solar Observatories

Dedicated instruments continuously monitoring the Sun at radio frequencies include, among many others, the ground-based distributed Callisto network (Benz et al. 2009) and satellite-based instruments like the WAVES instrument aboard the WIND satellite close to L1 (Lepping et al. 1995), and the SWAVES instrument aboard the STEREO-A satellite (Kaiser 2005).

The Callisto network to date consists of more than 220 individual instruments distributed around the globe of which on average more than 80 provide public (open source) radio spectrograms from continuous solar monitoring on a daily basis (Monstein et al. 2023). Their data contain sweeps of 200 frequencies taken in 0.25 s intervals in the native frequency range covering 45→870 MHz, while some dedicated instruments cover 10→80 MHz and others 1045→1600 MHz using heterodyne converters. We find that the best overlap with RNO-G in global position, data availability, and frequency range is provided by the HUMAN observatory in Belgium (Marqué et al. 2008), which is one of the Callisto instruments.

The SWAVES instrument is part of the STEREO satellite mission (Bougeret et al. 2008). STEREO consisted of two satellites revolving around the Sun ahead of (STEREO-A) and behind (STEREO-B) Earth's orbit. Although the STEREO-B mission concluded in 2014, STEREO-A is still operational and provides publicly accessible averaged spectrograms with minute binning that cover frequencies up to 16 MHz. STEREO-A's orbital velocity is faster than Earth's; it lagged behind Earth by 50° when RNO-G started operation in June 2021, overtook Earth in August 2023 and will lead by 50° by 2026. A large fraction of the solar disk is therefore simultaneously observed by both SWAVES and from terrestrial observatories.

There are several other dedicated solar observatories, such as the instruments flying on-board the Parker Solar Probe, e.g. Bale et al. (2016). Their data, however, was less readily available as a reference for RNO-G data. Dedicated solar observatories, both existing as well as proposed e.g. Gary et al. (2023), naturally have more targeted abilities to monitor the Sun. By contrast, although solar science is ancillary for instruments such as LO-FAR (van Haarlem et al. 2013), the capabilities when dedicated observing time is used to point at the Sun can provide unprecedented detail e.g. Morosan et al. (2019). These instruments are however not specialised in delivering continuous (almost real-time) data for identifying radio flares in the Earth's field of view.

2. Identifying solar flares in RNO-G

The RNO-G instrument, although not originally designed for solar observations, nevertheless has several unique capabilities that can inform our understanding of flares. Primary among these is the high (3.2 GSa/s) sampling rate and broadband frequency

response, favoring data collection in the time domain. By contrast, typical solar observatories integrate power over a range of pre-defined frequencies in time increments of order 1-10 ms. RNO-G can therefore uniquely probe impulsive radio emissions on nanosecond time scales. Since RNO-G strives for a continuous up-time to maximize neutrino livetime, the reliance on solar power provision ensures that RNO-G will be sensitive to flares whenever the Sun is above the horizon.

We now discuss our identification of solar flares and analysis of those events.

2.1. Elevated trigger rates

Rather than continuously writing data to disk, RNO-G does so only when a trigger is issued. To prevent high-rate noise backgrounds from clogging the RNO-G data stream, the trigger thresholds are self-adjusting to keep a constant trigger rate. Several sources of transient noise phenomena that are capable of triggering the stations include:

- Transient noise sources originating from the station itself, which constitute part of the ‘ambient’ background and are not expected to lead to elevated trigger rates in the stations. Such noise sources include self-induced noise from the stations’ power and communication systems, which was present in early data but was suppressed with subsequent hardware and electronics improvements.
- Tribo-electric discharge during periods of high wind periods are known to cause elevated trigger rates (Aguilar et al. 2023).
- The radiosonde from twice-daily weather balloon flights telemeters data at 403 MHz. Depending on the flight trajectory, the weather balloon signals occasionally have an impact on the trigger rates of individual stations.
- Flights to/from Summit Station and commercial airplanes flying overhead emit unintentional and intentional (such as radio altimeters to determine their height above ground) radio signals. Depending on height and proximity, they can trigger multiple stations.
- Local Radio-Frequency Interference (RFI) generated by human activity slightly elevates the overall background rate for the 1–2 stations closest to the main building of Summit Station (or whenever field work is conducted at other locations), but its impact will diminish with increasing distance.

The lowest-level indicator of solar flaring activity is, therefore, a coherent increase in the trigger rates (as well as the recorded RMS voltages) across all stations. Each RNO-G station has two main trigger conditions, corresponding to trigger formation in either the deep Vpol antennas (2/4 majority coincidence for the four deepest dipoles on the power string, see Figure 1) or the surface LPDA antennas (2/3 majority logic for the three upward-pointing LPDAs). To identify a sharp increase in the overall station trigger rates characteristic of solar flares, we use the excess metric given by Li & Ma (1983),

$$S = \sqrt{2} \left[N_{\text{on}} \cdot \ln \left(\frac{(1 + \alpha) N_{\text{on}}}{\alpha (N_{\text{on}} + N_{\text{off}})} \right) + N_{\text{off}} \cdot \ln \left(\frac{(1 + \alpha) N_{\text{off}}}{N_{\text{on}} + N_{\text{off}}} \right) \right]^{1/2} \quad (2)$$

to define a summed trigger rate excess in a sliding time window, where N_{on} is the summed number of events in all stations over a three second time interval, N_{off} is the local background rate

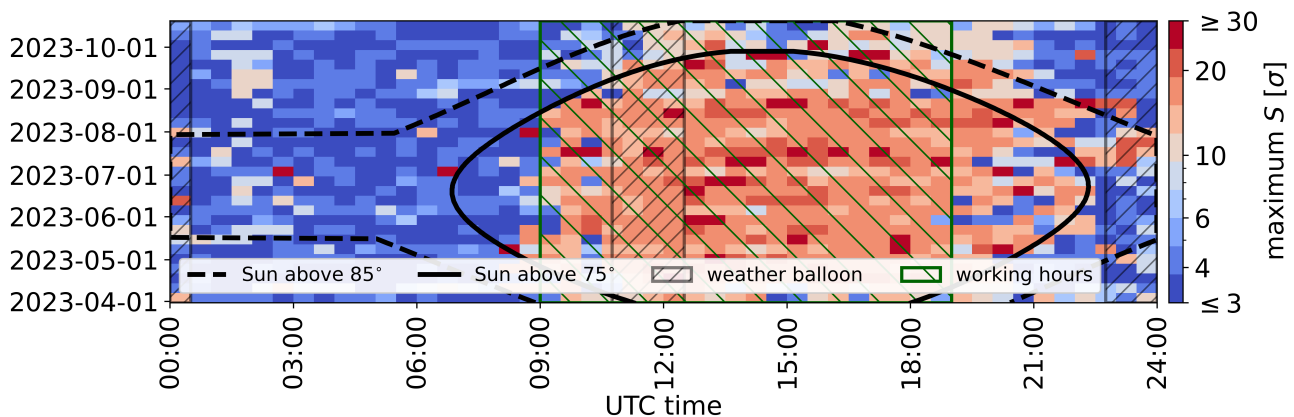


Fig. 3. Deep trigger rate excesses (maximum recorded per week and daily half hour) observed in the RNO-G array as a function of time-of-day and time-of-year, illustrating the correlation with solar elevation. We note no obvious increase in trigger rates during balloon flights (grey hatched areas), but a clear enhancement of excesses during sunlight hours. However, most trigger rate enhancements are due to sources other than the Sun, given that also human activity is also maximal at such times. This is particularly visible in the bias towards local evening hours. Normal working hours at Summit Station last from ~ 7 am to ~ 5 pm local time (green hatched areas).

of all stations over a 5 minute window around the on-time, and $\alpha = 0.01$ the ratio of signal and background integration time. In the ideal case of zero signal contribution in the off-region, the value of S would thus correspond to an excess significance in terms of σ over the ambient background (Li & Ma 1983). Underfluctuations in the local background rate, e.g. due to stalled data-taking or the dynamic threshold adjustments, are masked by the daily average background rate to avoid artificial increases of the excess metric S . The excess metric was formed separately for the surface LPDA antenna trigger and the in-ice Vpol trigger, and showed higher variability due to anthropogenic backgrounds for the surface component. The surface trigger rate was therefore not used for selecting our solar flares sample. The maximum values obtained for the excess metric S as a function of time-of-day and day of the year for the in-ice Vpol antenna triggers are shown for the 2023 season in Figure 3. It is evident that event trigger clusters are more prominent during the daytime, presumably linked to human activity; this, of course, coincides with times when the Sun’s sky location reaches its maximum elevation above the horizon. Therefore, elevated trigger rates, although expected, are not a sufficient criterion to identify solar flares in RNO-G. More sophisticated search strategies are needed, in particular exploiting temporal correlations with data from dedicated solar observatories.

2.2. Correlations with dedicated solar observatories

We use the trigger rate excess metric S from Equation 2 to search for solar flare events in the RNO-G data and estimate the efficiency with which solar flare events are recorded by the RNO-G stations. For this purpose, we use publicly available data from Callisto (Benz et al. 2009) and SWAVES (Bougeret et al. 2008).

As shown in Figure 4, we investigated all trigger rates excesses S in RNO-G over 3 minute time-windows. Without considering any correlation with solar events, the maximum excesses for the entire data taken in 2022 and 2023, respectively, follow the distribution shown in blue. Callisto publishes a list of identified burst times and observatories that did see an excess in their spectrograms. Burst times are reported with minute-precision which motivated the 3 minute size of the time window for the analysis. Selecting those periods where the calcu-

lated excess exceeds $S > 13\sigma$ to all Callisto bursts identified by HUMAIN (orange) retains only 2% of this distribution and allows us to identify a solar burst-enhanced sample. It is found that the HUMAIN referenced sample has a fractionally larger number of high trigger rate excursions. The predefined 2% accidental coincidence level cut is surpassed by 26 HUMAIN flares in 2022 and 49 flares in 2023. Neglecting the few per-cent contamination in the classification of events, we infer that RNO-G recorded a total of 75 flares that caused a statistically significant number of triggers in the summers of 2022 and 2023.

To strengthen this conclusion, an additional correlation with SWAVES is performed. Although only recording data at a maximum frequency of 16 MHz, and therefore below the nominal RNO-G turn-on frequency, the instrument has the advantage that it continuously monitors the Sun with constant sensitivity and is free of transient local RFI backgrounds. Hence, a sample of the largest SWAVES excesses (>15 dB) is selected and cross-matched with RNO-G to get an estimate for the detection efficiency of bright solar flares. In the complete 2022 and 2023 data, the SWAVES minute-binned data showed 119 excesses beyond 15 dB at 16 MHz during which RNO-G was actively recording data. Out of these, 53 flares showed an excess in the RNO-G trigger rates coincident with the flare time.

As shown in Figure 5, RNO-G detects a rise in trigger rates in roughly 60% of solar flares that occur when the Sun is higher than 10° above the horizon. For lower solar elevation angles, the efficiency drops, which can be explained by the fact that the Fresnel coefficients for transmission into the ice decrease significantly at grazing incidence angles. Due to the different bands and locations of SWAVES and RNO-G, a direct comparison of flare strength and RNO-G trigger likelihood on an individual event basis is challenging.

2.3. Event signatures

Solar flares with strong radio-frequency emissions have been historically classified and distinguished by their dynamic spectral characteristics and duration.

The RNO-G data contain a complete temporal record of each triggered event, which is thus more information than typical dynamic spectra, for which the phase information is discarded. In

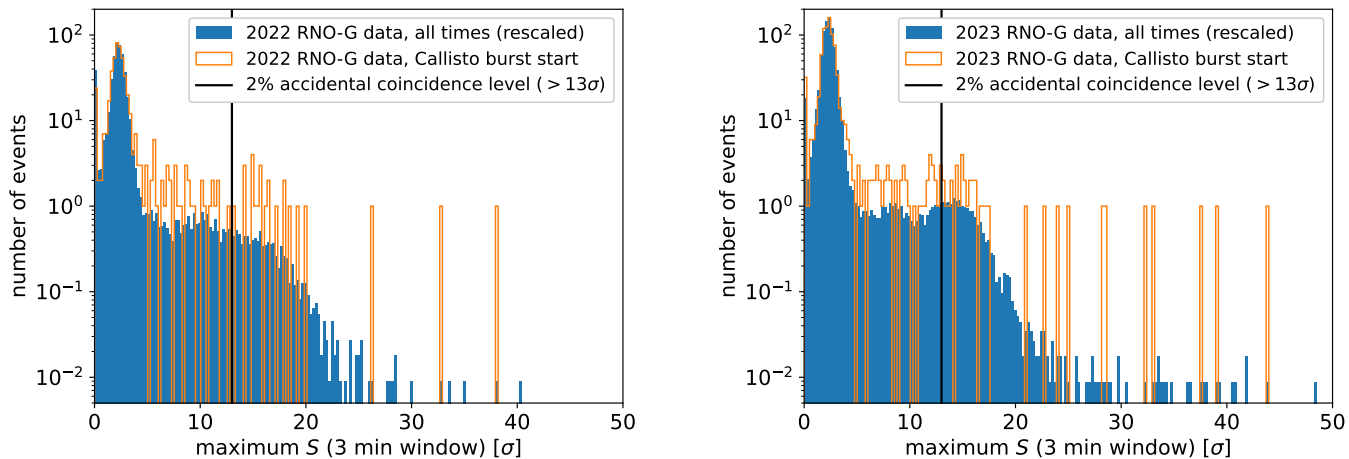


Fig. 4. Deep trigger rate excess for 2022 (left) and 2023 (right) in all RNO-G stations during three minute periods around solar flares identified by the Callisto network. The cut indicates a 2 percent chance of a random excess generated by different backgrounds.

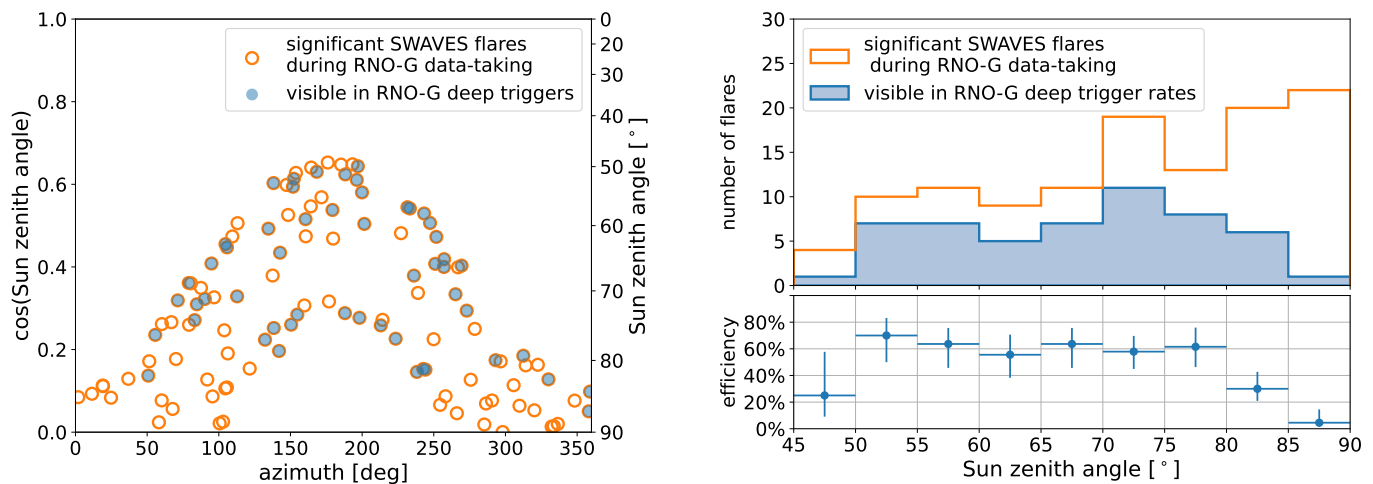


Fig. 5. Left: Flares detected in SWAVES (open circles) and RNO-G (filled circles) as a function of local zenith and azimuth at the RNO-G site. Right: Number of flares as function of local zenith. The orange lines show all flares that RNO-G could, in principle, have observed, while the blue curve shows the flares for which RNO-G observed an excess in the trigger rates. The RNO-G solar flare triggering efficiency in different regions of local zenith is shown below.

principle, RNO-G data could be used to independently search for solar flares by calculating continuous dynamic spectra, as is standard for other solar observatories. However, due to noise sources, as discussed above, this is not trivial and the identification of the flares considered in this article was facilitated by association of RNO-G data with data from dedicated solar observatories. We note that this is not a requirement. However, a dedicated RNO-G solar reconstruction pipeline would be necessary as dynamic spectra over time-scales of minutes are not required for neutrino searches, where nanosecond-scale excursions are relevant.

We do note that solar flares have been found in algorithmic studies for neutrino searches. Using for instance the machine learning method of anomaly detection (Meyers et al. 2023), it was found that waveforms recorded during solar bursts are considered anomalous compared to thermal noise dominated waveforms. A dedicated model was trained that identified a number of additional solar bursts (when comparing with data from other observatories), but the method also produced a large number of

false positives (i.e. anomalies not related to the Sun due to the small set of labelled training data), so that it was not considered a conclusive identification strategy at this point for stand-alone solar analyses, but something to be refined with more detected flares in the future.

The brightest flare observed in RNO-G thus far, which is easily identified by an elevated trigger rate, as well as in the anomaly search (or even by eye), is shown in Figure 6. This figure shows both the dynamic spectra of the LPDAs (more sensitive to signals coming from above) and the ~ 100 m deep Vpol antennas used for triggering. The time-dependence of the enhanced trigger rate is shown, which coincides precisely with the expectation from HUMAN. The LPDAs register both the strong initial Type III burst, as well as the subsequent Type II ring-down of the frequency spectrum. The deep antennas, however, only register the initial burst, since the signal both has to traverse 100 m of ice and reaches the antennas in an unfavorable geometry.

We provide a gallery for the subset of identified flares which we use for reconstruction in section 3 at <https://rnog->

solar flare on 2022-09-29 (RNO-G Sun zenith angle: 78.8 deg)

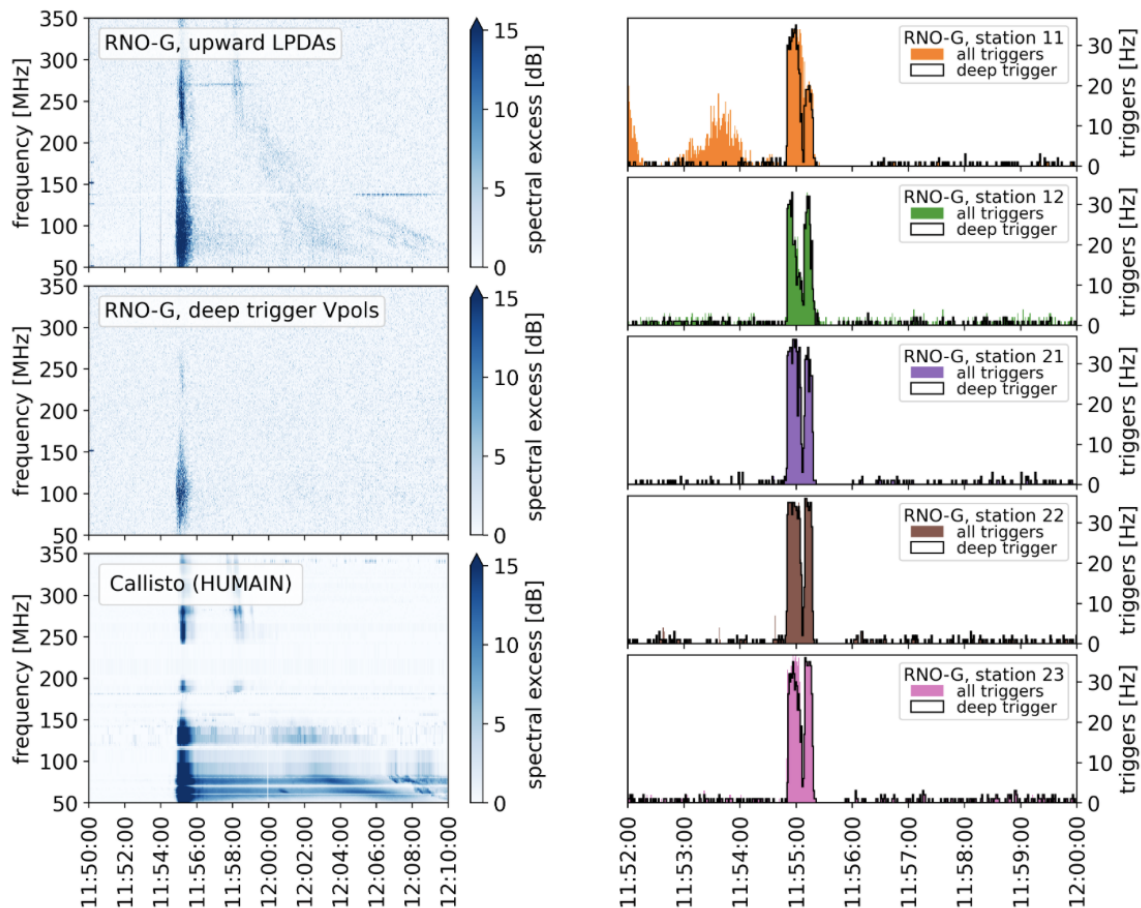


Fig. 6. *Left:* Frequency spectra from all active RNO-G stations observed in the surface LPDA channels (top) and in the ~ 100 m deep Vpol antennas used for triggering (bottom), as well as from the Callisto observatory HUMAN (Belgium) during the 2022-09-29 solar flare. *Right:* Deep and shallow trigger rates in all stations taking data during the flare. In all cases, the trigger rates quickly saturate at the flare onset; rates relax slightly as the flare temporarily weakens and the servo raises the station trigger thresholds, then saturate again as the flare re-intensifies.

data.zeuthen.desy.de/solarflares. As expected from the statistics of Callisto flares, and because the method used for detection is tailored towards sudden increases in the trigger rates, the majority of these flares are of type III, sometimes with several subsequent distinct emission spikes.

3. Reconstructing the flare direction

As opposed to data from solar spectrographs, like HUMAN, every vertical line in the dynamic spectrum from RNO-G is calculated from one waveform recorded in the time-domain, as shown in Figure 7. These same data therefore allow us to reconstruct the position of the emission as observed with RNO-G. For the RNO-G neutrino mission, such a reconstruction is highly relevant to provide absolute pointing, calibration of the positions of the antennas, and an illustration of the achieved resolution on the signal arrival direction.

For the purpose of this section, we selected a subset of 21 ‘highly-impulsive’ flares as identified by the SWAVES and Callisto correlation with RNO-G data, to study the reconstruction performance. These flares were chosen on the basis of the highest amplitude of the coherently summed waveform for the in-ice Vpol channels.

3.1. Expected position resolution and direction

The expected solar reconstruction resolution is determined by three factors: knowledge about the location of the emission source on sky, the trajectory followed by the signals (“rays”) as they traverse the air-ice boundary and are refracted into the ice, and the RNO-G instrument characteristics.

Typical solar flare spatial characteristics have been well-studied by dedicated radio-frequency observatories. Source locations on the Sun have been fixed by LOFAR, e.g., with typical resolutions of $O(10'')$ in angle; such high precision is largely attributable to the large number ($O(500)$) and spacing ($O(500)$ m) between receiver antennas used for interferometric reconstruction, affording strong constraints on the direction of incident signals. For RNO-G, the expected resolution is poorer, owing to (in order of importance): i) the meter-scale vertical, and 10-meter-scale horizontal separation between RNO-G receiver antennas, ii) the required correction for refraction at the air-ice boundary, iii) uncertainties in the positions of the antennas in-ice – although the surface location of the holes is determined to within 5 cm using high-accuracy GPS, possible hole-tilting during drilling is not monitored, so lateral deviations of the in-ice antennas relative to the surface of order 10-20 cm are possible, iv) uncertainties in the refractive index profile in the ice.

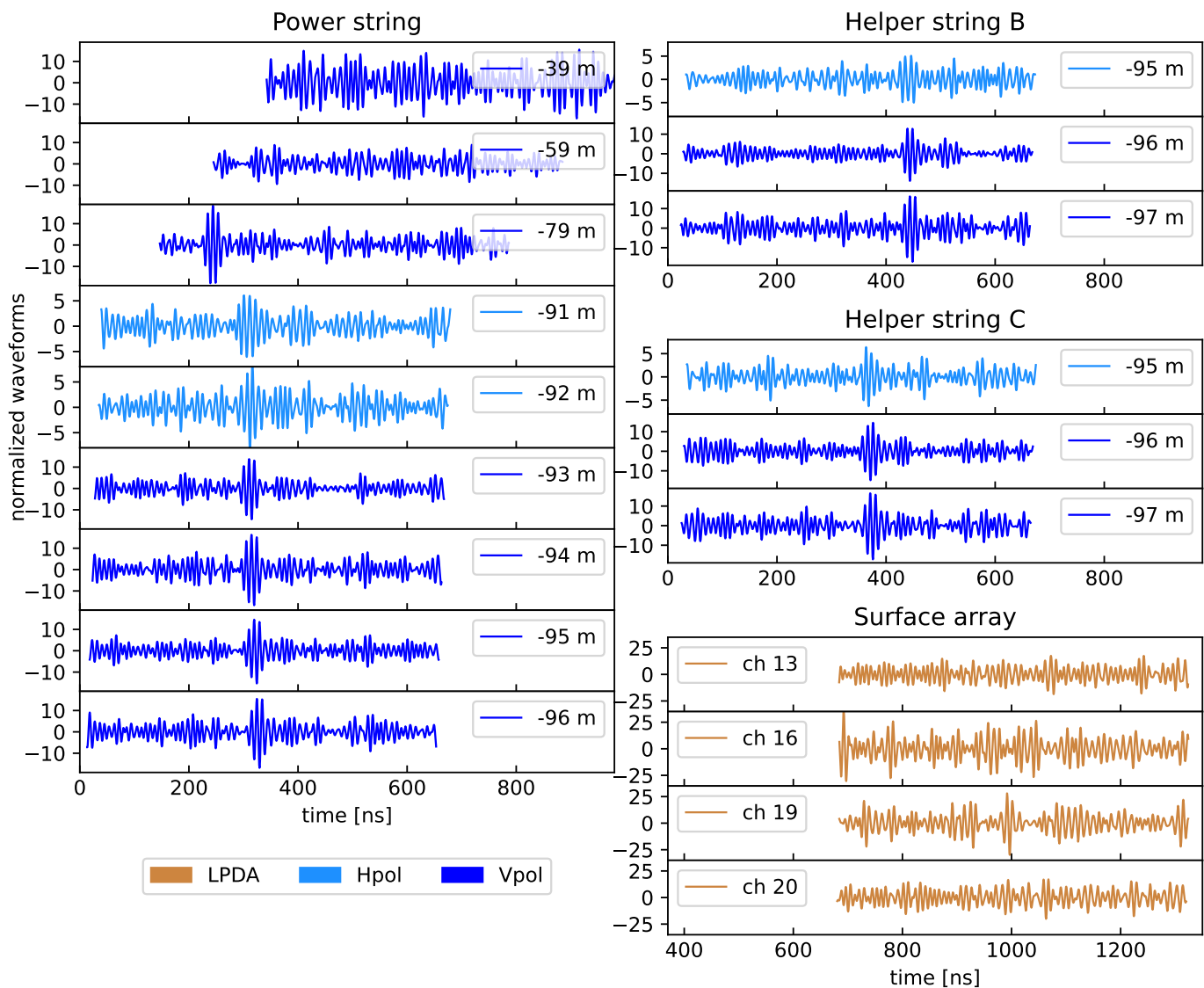


Fig. 7. Waveforms for one event recorded in RNO-G during the September 29, 2022 solar flare. The vertical axis shows the signal-to-noise ratio (SNR) in a given channel, normalized to the ambient thermal noise level pre-flare. Each channel’s start time has been offset, relative to the Vpol at -96 m (power string), by an amount equal to the cable delay, to show the true signal arrival time at the location of that channel. The evident peak signal arrival time in the shallower Vpol at -79 m, for example, is approximately 80 ns earlier than Vpol at -93 m, as expected for a down-coming plane wave incident from the Sun, given the depths of the two channels. Signals in Vpols at -39 m and -59 m arrive too early in the buffer to be captured at the time when the deep channels initiate the DAQ trigger latch. Similarly, signals arrive at the surface LPDAs (orange) approximately one-half microsecond earlier than the deep in-ice channels; post-peak data are captured hundreds of nanoseconds after the actual signal has already swept through those channels. Surface LPDA channels 13, 16, and 19 point upwards, rotated by 120 degrees azimuthally (and therefore have different gains in the direction of the Sun), while LPDA channel 20 (shown for illustration) points downwards, and sees correspondingly less flare signal. For this reason, the remaining 5 downward-pointing LPDA channels are omitted in this figure.

Since RNO-G has performed extensive measurements of all relevant cable delays (nominally quoted to a precision of several hundred picoseconds), uncertainties in propagation times through the DAQ are a sub-dominant effect. Similarly, the relative timing of wavefronts passing through two antennas is also determined to an accuracy of order 100 picoseconds; this is particularly true of solar flares, as the entire 500 ns of a typical waveform trace contains an RF imprint of the emission. The time delay uncertainty results in an angular uncertainty of about 0.2 degrees, if antennas from different strings are used that are sufficiently distant from each other.

The combination of these effects results in an expected source location resolutions of order one degree, roughly corre-

sponding to the solar-spot size in the sky at RNO-G frequencies (see Section 1.2). This value is comparable to previous South Polar solar flare reconstructions (Allison et al. 2018). Note that the hundreds-of-MHz frequency regime to which RNO-G is sensitive favors emission regions close to the surface; coronal plasma ejection away from the surface and into the photosphere favors longer-wavelength (decameter, e.g.) portions of the spectrum.

3.2. Interferometric reconstruction

Figure 7 shows the time-domain waveforms recorded during the solar flare on September 29th, 2022, which clearly illustrates the increasing delay of the voltage peak for the deeper antennas in

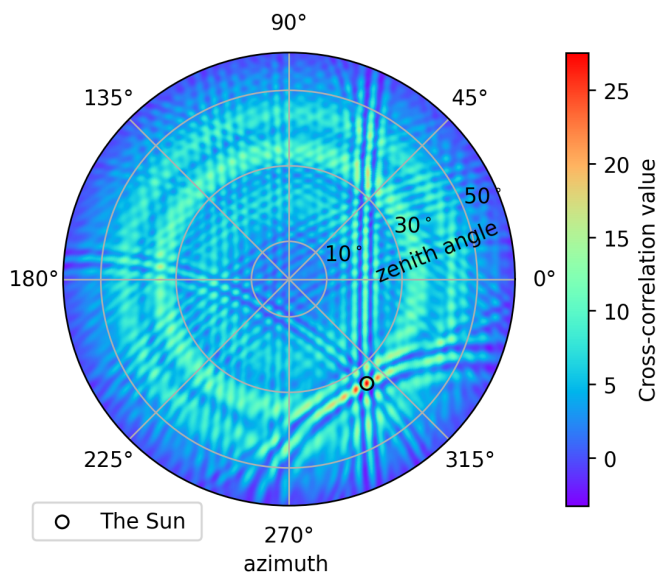


Fig. 8. Interferometric sky map for one set of station 11 waveforms recorded during the flaring Sun on September 29, 2022. Circle indicates the maximum pixel for this event, which is taken as the measured solar location on the sky (not corrected for refraction). Color scale indicates the cross-correlation value for a given pixel.

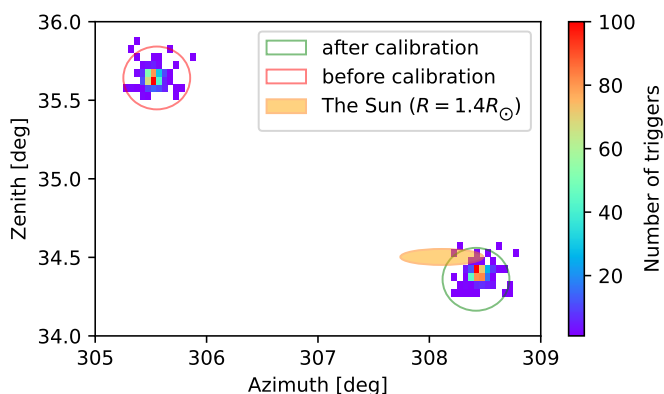


Fig. 9. Reconstructed source location for the solar flare of September 29, 2022, zoomed in as compared to Figure 8. The reconstruction results before and after calibrating the antenna positions of station 23 are shown. The size of the Sun is chosen as the radio spot size of the Sun, corrected for refraction at the air-ice boundary.

a given string, and is the signature of a plane wave propagating downwards through the array.

It should be noted that, for the flares presented in this work, the firmware of the instrument was not capable to in-situ correct for the time-delays between LPDA and Vpol/Hpol channels due to the drastically different length of cables. This means that all antennas are read-out, but the signals are not causally related due to the travel time. Thus, no concurrent recordings in all channels are present for this year of observation and LPDA and Vpol/Hpol triggers have to be analyzed separately.

The standard RNO-G source reconstruction codes, designed for both cosmic ray as well as neutrino reconstruction, are based on interferometry of the signals recorded in the time-domain. For this study, we use the software framework NuRadioReco (Glaser et al. 2019) for the interferometric reconstruction of the signal arrival direction of solar flare events. The time delays that maxi-

mize the total cross-correlation between all possible Vpol (pairwise) combinations are directly translated into a most-likely signal arrival direction in both elevation and also azimuth. To calculate this total cross-correlation, we only sum over the pairwise cross-correlation between the Vpols at ~ -80 m and below, since the expected arrival time for a downward propagating signal lies outside the recorded time-window for the higher-up antennas.

A single interferometric map calculated for the waveforms depicted in Figure 7 is shown in Figure 8. For each captured event, the brightest pixel in a zoomed (± 5 degrees from the known solar location) interferometric map is recorded. The reconstructed source location, for all events recorded during the flare in one typical station, is presented in Figure 9. We observe a deviation, relative to the known solar position at a given time, of approximately 2 degrees in azimuth and one degree in elevation. The remaining RNO-G stations also show discrepancies of $\sim 1-2$ degrees in both coordinates, which emphasizes the need for the calibration of the absolute pointing of RNO-G.

3.3. Geometry calibration and systematic uncertainties

Consistent with the interferometric reconstruction approach, antenna positions are calibrated in RNO-G relative to each other. Starting from nominal installation positions (known depth based on the measured length of the string, but less well-known azimuthal orientation due to absolute borehole position and inclination uncertainties), signals from embedded local calibration pulsers are used to initially refine the tabulated receiver antenna positions. Fine-tuning requires absolute pointing to distant external sources such as the Sun.

Starting with the observed deviations between the reconstructed and the known solar positions, we have used a minimization code to extract the antenna coordinates which give the best match to the known solar location in the sky at any given time. For this minimization, we assume that the relative cable delays are known; the refractive index profile as function of depth $n(z)$ is drawn from Oeyen et al. (2023), although we later toggle the $n(z)$ profile by $\pm 1\%$, and obtain consistent results. We also find that our results are relatively insensitive to cable delay uncertainties of order ± 0.2 ns. Our fitting procedure is significantly over-constrained – for each of the 21 flares used for the minimization, there are approximately 50–500 reconstructable independent events, often spread across a time interval large enough that the Sun drifts 2–3 degrees in the sky.

This minimization procedure yields individual shifts of order 10–20 cm in (x,y) for the in-ice antennas, with much smaller shifts obtained in depth (z) . Although the antennas were shifted individually, the resulting horizontal displacements of the antennas from one string were approximately the same. Sub-dividing the solar flares into two sub-samples significantly degrades the statistical precision, but allows us to estimate systematic errors that are approximately half the size of the calculated shifts (5 cm, obtained as the width of the distribution of the difference in post-calibration positions for the two subsamples). The obtained position shifts in (x,y) are somewhat larger than the expected uncertainty in the GPS-obtained antenna string positions, however, such shifts are commensurate with possible deviations from verticality during drilling and are in agreement with local pulser calibration, as shown in (Aguilar et al. 2024). After calibration, both the solar azimuth and elevation reconstructions improve considerably relative to the nominal solar position. We also note that we can easily track the motion of the Sun in the sky, as shown over the 8-minute duration of the 12th of July, 2023 solar flare (Figure 10 and 11). As shown in Figure 9 the Sun is comparable

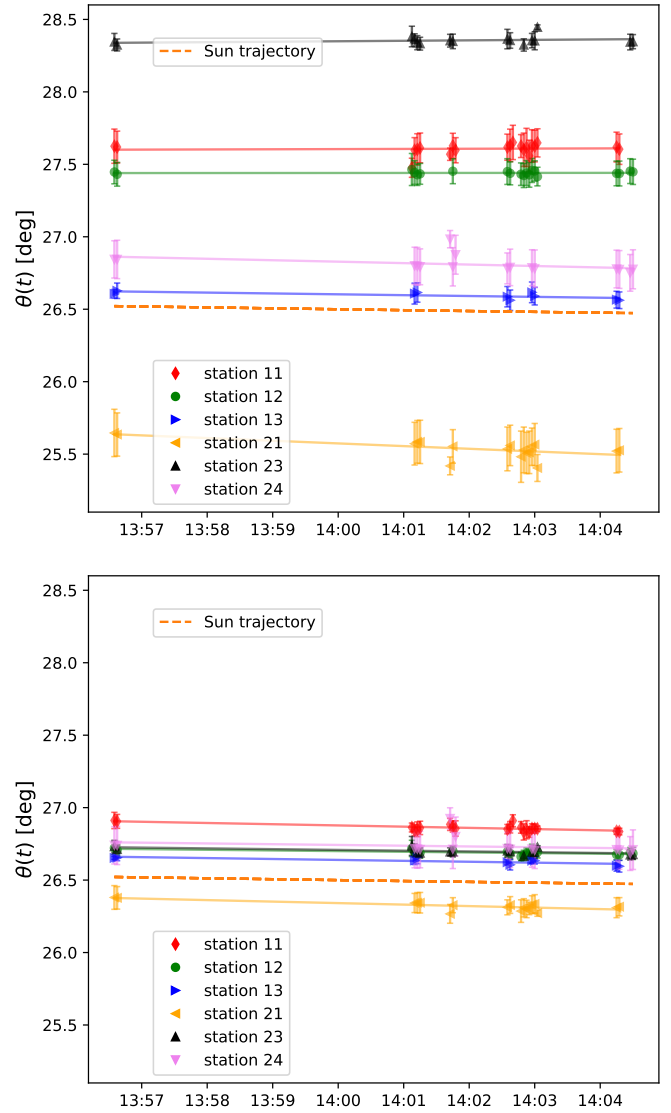
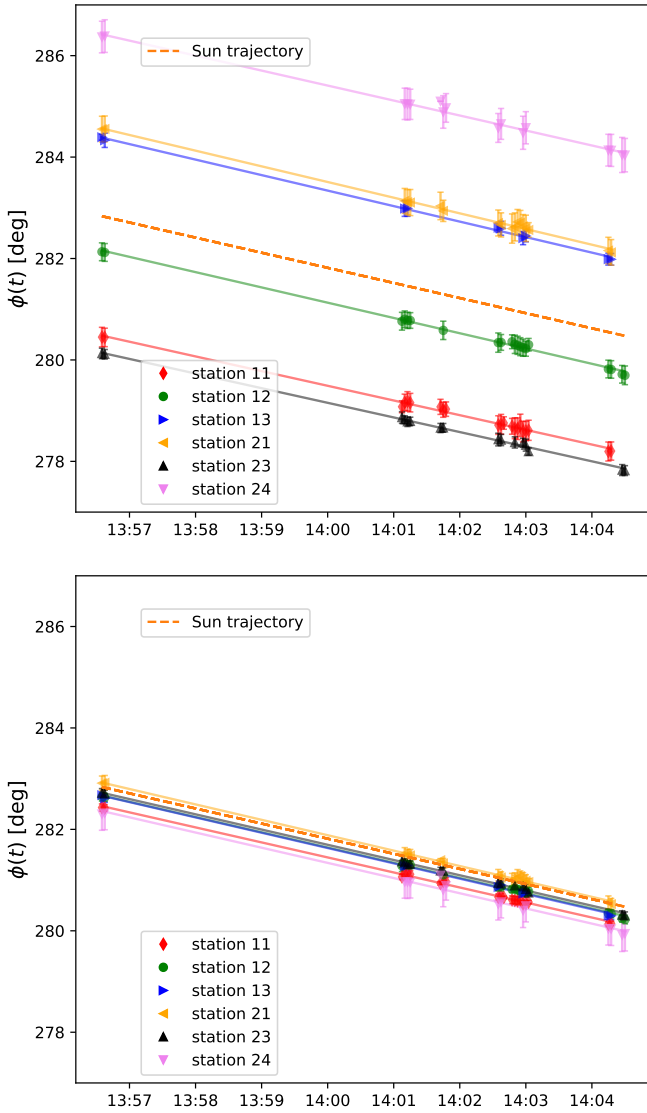


Fig. 10. Reconstructed azimuth angle versus time for the solar burst recorded on July 12th, 2023 before (top) and after applying the calibration of the antenna positions (bottom). Markers indicate times at which the recorded signals allowed for an accurate pointing of the Sun. Also indicated is the expected trajectory of the Sun (dashed line, no markers). Due to a high trigger threshold, station 22 did not record enough data during the flare to reconstruct the source direction.

in size to the RNO-G angular resolution. Although solar flares typically do not originate from the center of the Sun (resulting in a corresponding inherent uncertainty in the source location), we assume a central emission point in the absence of more precise information. After further refinement of the calibration and with more input from external observatories, we anticipate that a true offset from the solar center (as visible in Figure 9) may be measured for future flares. We note that, although each individual fitted event is constrained to reconstruct at the location of the Sun by fiat, the calibrated antenna coordinates will vary flare-to-flare, event-to-event and station-to-station. For the final comparison of the known solar location with our reconstruction, we take the average positional shift per channel, which, when applied to our flare sample, will no longer necessarily reconstruct to the center of the Sun.

Fig. 11. Same as Figure 10, but for reconstructed zenith angle. Note that not all flares can be reconstructed in all stations.

4. Time-domain characteristics of signal shapes recorded during solar flares

As evident in Figure 7, we observe transient (of order 10 ns) signals in our waveforms, indicative of acceleration at the source, on a similar time scale. We stress, however, that the recorded time-domain waveforms include dispersive effects from the ionosphere (discussed below), the antenna itself, and the data acquisition system, for which we have not corrected here. To quantify how often such impulsive signals are apparent in our solar flare candidate waveforms, we constructed a two-dimensional plot of peak signal-to-noise ratio in an observed waveform vs. the signal duration, defined as the time duration between the signal onset (defined as the time at which the signal voltage envelope exceeded half-maximum and the signal falling edge (defined as the time at which the recorded signal voltage fell below half-maximum). Figure 12 shows this two-dimensional plot, and also shows the cut (black line) corresponding to those events which are more readily interferometrically reconstructed (blue) vs. those events for which the peak in the interferometric map is considerably weaker. Also, continuous-wave background gener-

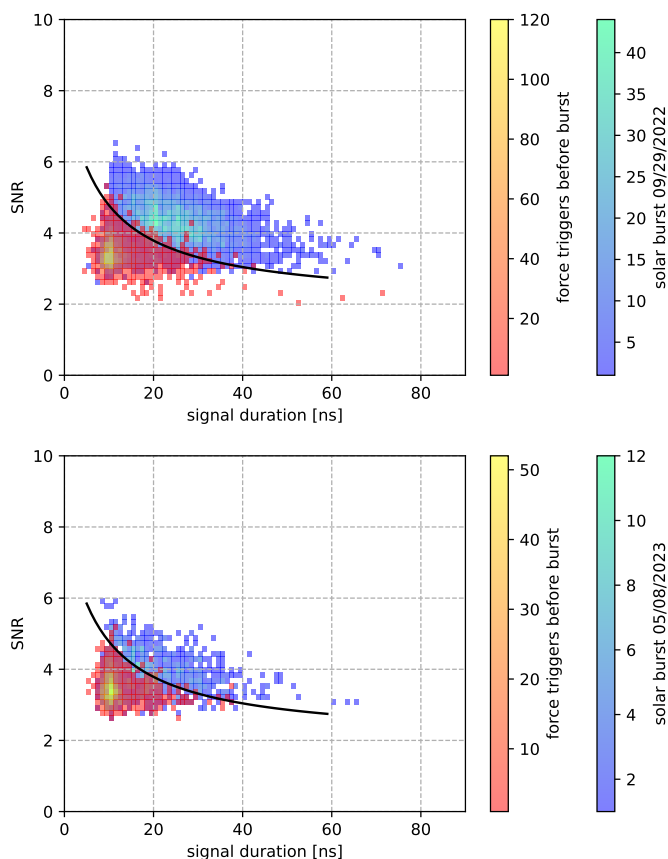


Fig. 12. Illustration of the impulsivity of the signals recorded. Signal-to-noise ratio (SNR) is shown as function of signal duration. The figure compares the noise signal recorded during normal operations (periodic forced triggers) with RF triggered signals recorded during the solar burst of September 29th, 2022 (top) and May 8th, 2023 (bottom). The area above the black line admits less than 1% of forced triggers, and is used to estimate the number of solar flare signals that are dissimilar from noise.

ally exhibits a signal-to-noise ratio of less than 2 and therefore falls below the cut line. Although our triggered data sample in the absence of solar flares is dominated by events close to the thermal noise floor, events also include impulsive anthropogenic backgrounds and therefore are less useful, compared to forced triggers, which are used as a reference sample. With this criterion, approximately 1/3 of the event triggers recorded during known solar flares produce observable impulsive signals in our receivers.

In principle, it should be possible to extract polarization from the time-domain signals, as has been demonstrated for cosmic-ray signals and in-ice sources (Anker et al. 2020, 2022). However, for broadband signals like those observed in RNO-G, ionospheric dispersion (as function of frequency) may play an important role for signals originating from outside the Earth’s atmosphere (Spoelstra 1983). In particular, at the low frequencies that RNO-G is operating at, the dispersive delays across the band can add up to several tens to hundreds of nanoseconds, depending on the state of the ionosphere. Without additional information about the ionosphere, it is therefore challenging to de-disperse the pulse and also correct for any polarization rotation that may be introduced during ionospheric propagation. For time integrated quantities the polarization calculation should be possible (Morosan et al. 2022) (as dispersion will mostly cancel out), however, this will not reveal characteristics of individual pulses,

as with cosmic ray or neutrino signals. Considerable additional work will therefore be needed to assess the utility of the RNO-G data for polarization measurements of solar emission, exploiting the entire bandwidth for the best results.

5. Conclusions

RNO-G radio observations of solar flares are both interesting, in that they reveal nanosecond-scale broadband acceleration mechanisms, and also useful, in that they afford a powerful, infinite-distance calibration source at a well-defined location on the sky. From a calibration standpoint, as demonstrated herein, after optimizing the coordinates of the receiver antennas, using the known position of the Sun in the sky as a constraint, both azimuthal and elevation reconstruction precision for above-surface sources approaches 15 arc-minutes. We have also shown in this paper that using the Sun as known position, we can achieve sub-degree absolute pointing on the signal arrival direction for all RNO-G stations viewing above-ice sources. Both reconstruction precision and absolute pointing are clearly adequate for cosmic ray reconstruction as well as neutrino reconstruction, although verification of the latter awaits reconstruction of dedicated in-ice transmitter sources, at ranges of hundreds of meters. The direction information of charged cosmic rays is intrinsically already smeared by magnetic fields to more than a degree from their sources and for neutrinos current arrival direction reconstructions estimate only a small fraction (less than 10%) to be reconstructed better than 1° statistical precision due to the dominant additional uncertainties from determining the position on the Cherenkov cone, not yet including systematic uncertainties.

We note that, in the approximately 50 station-months of RNO-G livetime, there have been a total of 75 solar flares identified in the RNO-G data stream. These are readily characterized by a sharp enhancement in both station trigger rates and also station signal power. These characteristics make it unlikely that solar flare are a considerable background to neutrino searches with RNO-G, which illuminate only one or two RNO-G stations with single, non-repeating pulses.

In contrast to the large RNO-G solar flare data sample already accumulated, the Radio Ice Cherenkov Experiment (RICE, Kravchenko et al. (2003)), which ran continuously at the South Pole from 2000-2011 (comprising 144 station-months of livetime), observed only the (extremely bright) X-28 November 4, 2003 flare. Although RNO-G fortunately has been commissioned close to solar maximum, we attribute the higher efficiency of RNO-G to the more favorable solar viewing angle – the more inclined signal angles typical of the South Pole result in more reflected signal power at the surface, and therefore suppressed efficiency of the in-ice triggers typical of experiments such as RICE.

RNO-G is currently still under construction and we have reported here only data from the first year of 7 stations. RNO-G is scheduled to reach 35 stations with a total of 840 antennas by 2026. Adapting reconstructions across multiple stations and carefully adjusting the trigger rate will lead to extremely high resolution spectra, as well as precision location of solar flares almost as a by-product of the ongoing neutrino observation program. Future modifications to the trigger contemplate real-time suppression of trigger-threshold adaptation to allow a non-constant trigger rate for candidate solar flares, which would then instead maintain a constant trigger signal threshold and better articulate the tail end of the solar light curve, and provide considerably larger data sets, as the Sun approaches solar maximum in the summer of 2024.

Acknowledgements

We are thankful to the support staff at Summit Station for making RNO-G possible. We also acknowledge our colleagues from the British Antarctic Survey for building and operating the BigRAID drill for our project.

We would like to acknowledge our home institutions and funding agencies for supporting the RNO-G work; in particular the Belgian Funds for Scientific Research (FRS-FNRS and FWO) and the FWO programme for International Research Infrastructure (IRI), the National Science Foundation (NSF Award IDs 2118315, 2112352, 2111232, 2112352, 2111410, and collaborative awards 2310122 through 2310129), and the IceCube EPSCoR Initiative (Award ID 2019597), the German research foundation (DFG, Grant NE 2031/2-1), the Helmholtz Association (Initiative and Networking Fund, W2/W3 Program), the Swedish Research Council (VR, Grant 2021-05449 and 2021-00158), the Carl Tryggers foundation (Grant CTS 21:1367), the University of Chicago Research Computing Center, and the European Research Council under the European Unions Horizon 2020 research and innovation programme (grant agreements No 805486, No 101115122 and No 101116890). We thank Fachhochschule Nordwestschweiz (FHNW), Institute for Data Science in Brugg/Windisch, Switzerland, for hosting the e-Callisto network.

References

- Aguilar, J. A. et al. 2021, JINST, 16, P03025, [Erratum: JINST 18, E03001 (2023)]
- Aguilar, J. A. et al. 2022, Journal of Glaciology, 68, 1234
- Aguilar, J. A. et al. 2023, Astropart. Phys., 145, 102790
- Aguilar, J. A. et al. 2024, in preparation, "Instrument Design and Performance of the first seven stations of RNO-G"
- Allison, P. et al. 2018, arXiv:1807.03335 [astro-ph.HE]
- Allison, P. et al. 2019, Nucl. Instrum. Meth. A, 930, 112
- Anker, A. et al. 2020, JINST, 15, P09039
- Anker, A. et al. 2022, JCAP, 04, 022
- Askar'yan, G. A. 1961, Zh. Eksp. Teor. Fiz., 41, 616
- Bale, S. D., Goetz, K., Harvey, P. R., et al. 2016, Space Sci. Rev., 204, 49
- Barwick, S. & Glaser, C. 2023, published in Neutrino Physics and Astrophysics, Encyclopedia of Cosmology II, arXiv:2208.04971 [astro-ph.IM]
- Bastian, T. S., Benz, A. O., & Gary, D. E. 1998, Ann. Rev. Astron. Astrophys., 36, 131
- Benz, A. O., Monstein, C., et al. 2009, Earth Moon and Planets, 104, 277
- Berezinsky, V. S. & Zatsepin, G. T. 1969, Phys. Lett. B, 28, 423
- Bougeret, J. L. et al. 2008, Space Sci. Rev., 136, 487
- Dulk, G. A. 1985, Annual Review of Astronomy and Astrophysics, 23, 169
- Engel, R., Seckel, D., & Stanev, T. 2001, Phys. Rev. D, 64, 093010
- Fletcher, L. et al. 2011, Space Sci. Rev., 159, 19
- Gary, D. et al. 2023, in BAAS, Vol. 55, 123
- Glaser, C., Nelles, A., Plaisier, I., et al. 2019, Eur. Phys. J. C, 79, 464
- Halzen, F. & Hooper, D. 2002, Rept. Prog. Phys., 65, 1025
- Kaiser, M. L. 2005, Advances in Space Research, 36, 1483
- Komesaroff, M. 1958, Australian Journal of Physics, 11, 201
- Kopp, G. 2016, Journal of Space Weather and Space Climate, 6, A30
- Kravchenko, I. et al. 2003, Astropart. Phys., 19, 15
- Kumari, A., Morosan, D. E., Kilpua, E. K. J., & Daei, F. 2023, A&A, 675, A102
- Lepping, R. P. et al. 1995, Space Sci. Rev., 71, 207
- Li, T. P. & Ma, Y. Q. 1983, Astrophys. J., 272, 317
- Mann, G. et al. 1999, A&A, 348, 614
- Marqué, C. et al. 2008, e-CALLISTO (HUMAIN), Royal Observatory of Belgium. DOI: 10.24414/nrdh-c565
- Maxwell, A. & Swarup, G. 1958, Nature, 181, 36
- Meyers, Z. S. et al. 2023, PoS, ICRC2023, 1142
- Monstein, C., Csillaghy, A., & Benz, A. O. 2023, CALLISTO Solar Spectrogram FITS files [Data set]. International Space Weather Initiative (ISWI). DOI: 10.48322/pmwd-mk15
- Morosan, D. E. et al. 2019, Nature Astronomy, 3, 452
- Morosan, D. E. et al. 2022, Solar Physics, 297, 47
- Oeyen, B., Aguilar, J., et al. 2023, PoS, ICRC2023, 1042
- Plaisier, I., Bouma, S., & Nelles, A. 2023, Eur. Phys. J. C, 83, 443
- Spoelstra, T. A. T. 1983, A&A, 120, 313

- Stecker, F. W. 1973, Astrophys. Space Sci., 20, 47
- van Haarlem, M. P. et al. 2013, Astron. Astrophys., 556, A2
- Waxman, E. & Bahcall, J. N. 1999, Phys. Rev. D, 59, 023002
- Wentzel, D. G. 1984, Solar Physics, 90, 139
- Wild, J. P. & McCreedy, L. L. 1950, Australian Journal of Scientific Research A Physical Sciences, 3, 387
- Zas, E., Halzen, F., & Stanev, T. 1992, Phys. Rev. D, 45, 362

-
- ¹ University of Kansas, Dept. of Physics and Astronomy, Lawrence, KS 66045, USA
- ² Université Libre de Bruxelles, Science Faculty CP230, B-1050 Brussels, Belgium
- ³ Dept. of Physics, Center for Cosmology and AstroParticle Physics, Ohio State University, Columbus, OH 43210, USA
- ⁴ Dept. of Physics, Dept. of Astronomy & Astrophysics, Center for Multimessenger Astrophysics, Institute of Gravitation and the Cosmos, Pennsylvania State University, University Park, PA 16802, USA
- ⁵ Wisconsin IceCube Particle Astrophysics Center (WIPAC) and Dept. of Physics, University of Wisconsin-Madison, Madison, WI 53703, USA
- ⁶ Vrije Universiteit Brussel, Dienst ELEM, B-1050 Brussels, Belgium
- ⁷ Uppsala University, Dept. of Physics and Astronomy, Uppsala, SE-752 37, Sweden
- ⁸ Erlangen Centre for Astroparticle Physics (ECAP), Friedrich-Alexander-University Erlangen-Nürnberg, 91058 Erlangen, Germany
- ⁹ Vrije Universiteit Brussel, Astrophysical Institute, Pleinlaan 2, 1050 Brussels, Belgium
- ¹⁰ Dept. of Astrophysics/IMAPP, Radboud University, PO Box 9010, 6500 GL, The Netherlands
- ¹¹ Department of Physics, University of Maryland, College Park, MD 20742, USA
- ¹² Dept. of Physics, Dept. of Astronomy & Astrophysics, Center for Multimessenger Astrophysics, Institute of Gravitation and the Cosmos, Pennsylvania State University, University Park, PA 16802, USA
- ¹³ Deutsches Elektronen-Synchrotron DESY, Platanenallee 6, 15738 Zeuthen, Germany
- ¹⁴ Whittier College, Whittier, CA 90602, USA
- ¹⁵ Institut für Physik, Humboldt-Universität zu Berlin, 12489 Berlin, Germany
- ¹⁶ Dept. of Physics and Astronomy, Univ. of Nebraska-Lincoln, NE, 68588, USA
- ¹⁷ Dept. of Physics and Astronomy, University of Alabama, Tuscaloosa, AL 35487, USA
- ¹⁸ Dept. of Physics and Astronomy, University of Delaware, Newark, DE 19716, USA
- ¹⁹ Ghent University, Dept. of Physics and Astronomy, B-9000 Gent, Belgium
- ²⁰ Kapteyn Institute, University of Groningen, PO Box 800, 9700 AV, The Netherlands
- ²¹ Istituto ricerche solari Aldo e Cele Daccò (IRSOL), Faculty of Informatics, Università della Svizzera italiana (USI), CH-6605 Locarno, Switzerland

e-mail: authors@rno-g.org, steffen.hallmann@desy.de, masha.mikhailova@icecube.wisc.edu